University of Groningen

Organic aerosol formation and aging processes in Beijing constrained by size-resolved measurements of radiocarbon and stable isotopic ^{13}C

Ni, Haiyan; Huang, Ru Jin; Yao, Peng; Cosijn, Max M.; Kairys, Norbertas; Zhong, Haobin; Dusek, Ulrike

Published in:
Environment international

DOI:
10.1016/j.envint.2021.106890

IMPORTANT NOTE: You are advised to consult the publisher's version (publisher's PDF) if you wish to cite from it. Please check the document version below.

Document Version
Publisher's PDF, also known as Version of record

Publication date:
2022

Link to publication in University of Groningen/UMCG research database

Citation for published version (APA):
Ni, H., Huang, R. J., Yao, P., Cosijn, M. M., Kairys, N., Zhong, H., & Dusek, U. (2022). Organic aerosol formation and aging processes in Beijing constrained by size-resolved measurements of radiocarbon and stable isotopic ^{13}C. *Environment international*, *158*, Article 106890. https://doi.org/10.1016/j.envint.2021.106890

Copyright
Other than for strictly personal use, it is not permitted to download or to forward/distribute the text or part of it without the consent of the author(s) and/or copyright holder(s), unless the work is under an open content license (like Creative Commons).

The publication may also be distributed here under the terms of Article 25fa of the Dutch Copyright Act, indicated by the "Taverne" license. More information can be found on the University of Groningen website: https://www.rug.nl/library/open-access/self-archiving-pure/taverne-amendment.

Take-down policy
If you believe that this document breaches copyright please contact us providing details, and we will remove access to the work immediately and investigate your claim.

Downloaded from the University of Groningen/UMCG research database (Pure): http://www.rug.nl/research/portal. For technical reasons the number of authors shown on this cover page is limited to 10 maximum.

Download date: 15-03-2025

Environment International 158 (2022) 106890

Contents lists available at ScienceDirect

Environment International

journal homepage: www.elsevier.com/locate/envint

Organic aerosol formation and aging processes in Beijing constrained by size-resolved measurements of radiocarbon and stable isotopic ^{13}C

Haiyan Ni [a,b], Ru-Jin Huang [a,c,*], Peng Yao [b], Max M. Cosijn [b], Norbertas Kairys [b], Haobin Zhong [a], Ulrike Dusek [b,*]

[a] State Key Laboratory of Loess and Quaternary Geology, Key Laboratory of Aerosol Chemistry and Physics, Center for Excellence in Quaternary Science and Global Change, Institute of Earth Environment, Chinese Academy of Sciences, Xi'an 710061, China
[b] Centre for Isotope Research (CIO), Energy and Sustainability Research Institute Groningen (ESRIG), University of Groningen, Groningen 9747 AG, the Netherlands
[c] University of Chinese Academy of Sciences, Beijing 100049, China

ARTICLE INFO

Handling Editor: Hefa Cheng

Keywords:
Size-resolved aerosol
$PM_{2.5}$ pollution
Dual-carbon isotopes
Source apportionment
Fossil source contribution
Aqueous-phase chemistry

ABSTRACT

This study investigates the sources and atmospheric processes of size-resolved carbonaceous aerosols in winter 2018 in urban Beijing, based on analysis of dual-carbon isotopes (i.e., radiocarbon and the stable isotope ^{13}C). We found a size dependence of fossil source contributions to elemental carbon (EC), but no clear size dependence for organic carbon (OC). Comparable fossil source contributions to water-insoluble OC (WIOC; 55 ± 3%) and to water-soluble OC (WSOC; 54 ± 4%) highlight the importance of secondary aerosol formation, considering that fossil sources emit only small amounts of primary WSOC. OC concentrations increased during high $PM_{2.5}$ pollution events, with increased fossil and non-fossil WSOC concentrating at larger particles (0.44–2.5 μm) than WIOC (0.25–2.5 μm), highlighting the aqueous-phase chemistry as an important pathway for OC production. The ratio of $^{13}C/^{12}C$ (expressed as $\delta^{13}C$) of total carbon (−27.0‰ to −23.3‰) fell in the range of anthropogenic aerosol, reflecting small biogenic influence. $\delta^{13}C$ of OC increased with desorption temperature steps (200 °C, 350 °C and 650 °C). The strongly enriched $\delta^{13}C_{OC,650}$ (−26.9‰ to −20.3‰) and large mass fraction of $OC_{650°C}$ in total desorbed OC, both increasing with the increase of particle sizes, were caused by photochemical aging, especially during low and moderate $PM_{2.5}$ pollution events, when regional, aged aerosol played an important role. During low pollution events, higher $\delta^{13}C_{OC,650}$ and WSOC/OC ratios reflect a larger contribution and more extensive chemical processing of aged aerosol. In contrast, relatively low $\delta^{13}C_{OC,200}$ (−27.2‰ to −25.7‰) suggests the influence of secondary OC formation on the more volatile OC desorbed at 200 °C. $\delta^{13}C_{OC,200}$ was similar for all particle sizes and for different pollution events, pointing to an internal mixture of local and aged regional OC. Our results show that the organic aerosol in Beijing arises from a mixture of various sources and complex formation processes, spanning local to regional scales. Particle sizes < 250 nm show strong contribution from local secondary OC formation, whereas refractory OC in particles around 1 μm shows strong evidence for regional aging processes. In summary, primary emission, secondary and aqueous-phase formation, and (photo-) chemical aging all need to be considered to understand organic aerosol in this region and their importance varies with particle size.

1. Introduction

Fine particulate air pollution ($PM_{2.5}$, i.e., particulate matter with aerodynamic diameter ≤ 2.5 μm) in China is a serious environmental problem that is influencing air quality and human health as well as regional and global climate (Huang et al., 2014; Wang et al., 2014; Song et al., 2017; An et al., 2019). To effectively mitigate $PM_{2.5}$ pollution in China, considerable attention has been paid to investigating sources and atmospheric processes of carbonaceous aerosol, which constitutes the majority of $PM_{2.5}$ mass (Tao et al., 2017; Wu et al., 2018). Carbonaceous aerosol is usually quantified as total carbon (TC), which can be sub-divided into elemental carbon (EC) and organic carbon (OC) fractions.

* Corresponding authors at: State Key Laboratory of Loess and Quaternary Geology, Key Laboratory of Aerosol Chemistry and Physics, Center for Excellence in Quaternary Science and Global Change, Institute of Earth Environment, Chinese Academy of Sciences, Xi'an 710061, China (R.-J. Huang). Centre for Isotope Research (CIO), Energy and Sustainability Research Institute Groningen (ESRIG), University of Groningen, Groningen 9747 AG, the Netherlands (U. Dusek).
E-mail addresses: rujin.huang@ieecas.cn (R.-J. Huang), u.dusek@rug.nl (U. Dusek).

https://doi.org/10.1016/j.envint.2021.106890
Received 8 May 2021; Received in revised form 16 September 2021; Accepted 21 September 2021
Available online 1 October 2021
0160-4120/© 2021 The Authors. Published by Elsevier Ltd. This is an open access article under the CC BY-NC-ND license (http://creativecommons.org/licenses/by-nc-nd/4.0/).

EC and OC have distinct differences in thermochemical properties and atmospheric sources. EC is thermally refractory and inert in the atmosphere, while OC includes a large variety of organic species with different volatilities and is chemically reactive. EC originates mainly from incomplete combustion of fossil fuel and biomass. OC is directly emitted as primary OC (POC) from both combustion and non-combustion sources (i.e., biogenic OC) and is formed by gas-to-particle conversion in the atmosphere as secondary OC (SOC) (Pöschl, 2005; Hallquist et al., 2009; Zhang et al., 2015a). In addition, OC can be separated into water-soluble OC (WSOC) and water-insoluble OC (WIOC), and into more volatile and more refractory OC according to the thermal stability of OC. Recently emitted POC and newly formed SOC are usually more volatile than OC that is modified by photochemical processing in the atmosphere (Keller and Burtscher, 2017; Meusinger et al., 2017; Masalaite et al., 2020). Due to the complex composition and sources of carbonaceous aerosols, it is still challenging to quantify their sources.

The application of dual-carbon isotopes (i.e., radiocarbon ^{14}C and the stable isotope ^{13}C) to different carbon fractions in carbonaceous aerosols has proven to be a valuable tool to constrain sources and formation of carbonaceous aerosols (Ceburnis et al., 2011; Kirillova et al., 2013; Andersson et al., 2020; Ni et al., 2020; Zimnoch et al., 2020). ^{14}C analysis allows the direct quantification of the relative contributions from fossil (^{14}C-free) sources (i.e., coal combustion, vehicular emissions) versus non-fossil sources (e.g., biomass burning, biogenic emissions, cooking), based on the fact that carbonaceous aerosol of fossil origin does not contain ^{14}C. For example, Zhang et al. (2015b) found that during a severe winter haze, fossil sources contributed more strongly to OC in Beijing (~60%) than in Guangzhou (~40%), even though fossil sources contributed roughly equally to EC in both cities (~80%). Our recent studies in six Chinese megacities also found comparable fossil source contributions to EC in Beijing, Xi'an, Shanghai and Guangzhou (70–77%) during polluted days in winter, but large differences in fossil source contributions to EC in Chongqing (62%) and in Taiyuan (90%) (Ni et al., 2019a, 2019b). The stable carbon isotope ratio $^{13}C/^{12}C$ (reported as $\delta^{13}C$, see Eq. (1)) can shed light on both sources and atmospheric processing. $\delta^{13}C$ helps to further differentiate between types of fossil sources (e.g., coal combustion, vehicular emissions) or biomass burning (e.g., C3, C4 plant), because they have distinct ^{13}C source signatures (Mkoma et al., 2014; Andersson et al., 2015). In addition, $\delta^{13}C$ is also influenced by atmospheric processes via kinetic isotope effects. Previous studies have demonstrated that photochemical aging can lead to enriched $\delta^{13}C$ in the remaining organic aerosols (OA) due to a faster loss of isotopically lighter carbon (Kirillova et al., 2013; Pavuluri and Kawamura, 2016; Vodička et al., 2019). For example, $\delta^{13}C$ of WSOC arriving at an Indian Ocean receptor site was enriched by 3–4‰ compared to WSOC in the source regions due to aging processes during long-range transport (Kirillova et al., 2013). On the other hand, aerosol carbon originating from secondary OA (SOA) formation has a net depleted $\delta^{13}C$ relative to the precursors, if they are only partially oxidized (Fisseha et al., 2009; Iannone et al., 2010).

OC fractions desorbed at different temperature steps in helium roughly correspond to different OC volatilities, such that OC desorbed at lower temperature tends to be more volatile (i.e., less refractory) than OC desorbed at higher temperature. In a recent study, mass and $\delta^{13}C$ of more volatile OC and of more refractory (i.e., less volatile) OC were investigated in urban Lithuania (Masalaite et al., 2020). This study found that the mass fraction of more refractory OC was higher in summer than in winter due to active photochemical processing, and that in summer $\delta^{13}C$ of more volatile OC was more depleted relative to the more refractory OC, probably due to SOA formation. Moreover, Masalaite et al. (2018) found that vehicular emissions were a predominant source of the more volatile OC in the smallest particles (< 0.18 μm), whereas biomass burning was the most important source of more refractory OC in the large size range (0.32–1 μm).

Particle size changes with sources and transformations in the atmosphere, and it is an essential parameter determining health and climate effects of aerosol. Combustion sources typically emit primary ultrafine particles as well as gases that can promote ultrafine secondary particle formation. These small particles grow by condensation and coagulation during their residence time in the atmosphere to become larger accumulation mode particles, which have a low sedimentation rate and can be transported over long distance. Therefore, ultrafine particles are mainly of local origin and accumulation mode particles more of regional origin. However, the majority of studies on particulate matter in the urban environment focus on total $PM_{2.5}$. Very few studies focus on the sources of size-resolved aerosols, especially studies applying ^{14}C or ^{13}C analysis.

The aim of this study is therefore to analyze size-resolved aerosols during high, moderate and low $PM_{2.5}$ pollution events in Beijing, China. We aim to elucidate the sources and atmospheric processes of carbonaceous aerosols using the carbon isotopes ^{14}C and ^{13}C in different size ranges as well as in different carbon fractions of ambient aerosols for the first time. Comparing fossil source contributions to different carbon fractions (EC, OC, WIOC and WSOC) between larger accumulation mode and smaller particles can give important new insights into local vs. regional contribution to pollution events. Furthermore, $\delta^{13}C$ of size-resolved TC as well as different volatility OC fractions is used to reveal the role of secondary formation and aging in the atmospheric evolution of OC.

2. Methodology

2.1. Sampling

Size-resolved aerosol samples were collected at an urban background site in Beijing (see Table S1 of Supplementary Material for details), using a 5-stage high flow cascade impactor (flow rate = 100 L min^{-1}; Model 130, Copley Scientific). The cut-off sizes of the impactor were 2.5, 1.4, 0.77, 0.44, and 0.25 μm aerodynamic diameter (D_p). The particles with $D_p < 0.25$ μm were collected on a back-up filter. During the sampling, the impactor was located outside, so that particle size selection occurred at ambient temperature and RH. The 24 h samples were collected on pre-combusted quartz filters (90 mm diameter for back-up filters, 75 mm for stages of cut-off sizes 0.25 μm and higher; QM-A, Whatman Inc., Clifton, NJ, USA) from 10:00 to 10:00 the next day (local standard time, LST) from 29 December 2017 to 12 March 2018. After collection, filter samples were immediately removed from the sampler, packed in pre-combusted aluminum foils (450 °C for 3 h), sealed in polyethylene bags and stored in a −18 °C freezer.

2.2. Thermal-optical analysis of OC and EC

For back-up filters that uniformly collected particles with $D_p < 0.25$ μm, OC and EC mass concentrations were measured using a Sunset carbon analyzer (Model 5L, Sunset Laboratory, Inc., Portland, OR, USA) following the EUSAAR_2 thermal-optical transmittance protocol (Cavalli et al., 2010). During the analysis, the laser transmittance signal through the filter was monitored continuously for determination of the OC/EC split. The reproducibility determined by duplicate analyses of the back-up filters was within 5% for OC, 10% for EC. For the impactor stages with cut-off sizes 0.25 μm and higher, it is not possible to determine the OC/EC split point using the laser transmittance signal, because the impactor deposits on the filter are non-uniform. Therefore, only TC (=OC + EC) mass was measured with the Sunset analyzer, and OC and EC concentrations were estimated from the OC and EC extracted for ^{14}C analysis (see Text S1 for detailed explanation).

2.3. Analysis of carbon isotopes

For the analysis of carbon isotopes, six sets of impactor samples were selected to represent high, moderate, and low pollution events in Beijing (Fig. S1, Table S1): two 24 h samples collected during periods characterized by high $PM_{2.5}$ mass concentrations (175 μg m^{-3} and 142 μg m^{-3},

respectively), one 24 h sample representing periods with moderate $PM_{2.5}$ mass concentrations (77 μg m^{-3}), and one composite sample with relatively low $PM_{2.5}$ mass (~50 μg m^{-3}). The composite sample consisted of three 24 h impactor samples collected during time periods with similar $PM_{2.5}$ mass concentrations (difference within 15%) and similar back trajectories (Figs. S1 and S2). All selected samples had daily $PM_{2.5}$ concentrations higher than the median concentrations (33 μg m^{-3}) in the winter 2017/2018.

2.3.1. Stable carbon isotope analysis

The stable carbon isotope composition ($\delta^{13}C$; Eq. 1) was analyzed by coupling a Sunset carbon analyzer with an isotope ratio mass spectrometer (IRMS; 652 Optima, VG, Isoprime) via a custom-made interface to collect, purify and focus the sample (Dusek et al., 2013; Zenker et al., 2020). In brief, filter samples were placed in the front oven of the carbon analyzer, where the oven temperature was changed according to different temperature protocol settings. The manganese dioxide catalyst in the back oven of the carbon analyzer guaranteed the full oxidization of combustion products to CO_2. Then, the CO_2 sample from the carbon analyzer was dried with hygroscopic P_2O_5, purified and focused on two consecutive liquid nitrogen traps, further purified on the gas chromatography column (Varian CP7351, at room temperature), and entered the IRMS via a custom-made open split inlet.

TC was combusted from the filter samples following the EUSAAR_2 protocol (Cavalli et al., 2010). OC was thermally desorbed from the filter samples in a constant stream of helium, at three consecutive temperature steps of 200 °C, 350 °C and 650 °C (Zenker et al., 2020). A series of standards was measured every working day using one temperature step of 650 °C in helium, including the international reference material LVal (L-Valine, $\delta^{13}C = -24.03‰ \pm 0.04‰$; Schimmelmann et al., 2016) and two in-house standards CAF (caffeine, $\delta^{13}C = -38.2‰ \pm 0.10‰$) and CAN (caffeine, $\delta^{13}C = 0.61‰ \pm 0.10‰$).

$\delta^{13}C$ values are expressed in the delta notation as relative deviation from the international primary standard Vienna Pee Dee Belemnite (VPDB), and are usually reported in per mil (‰):

$$\delta^{13}C = \frac{\left({}^{13}C/{}^{12}C\right)_{sample}}{\left({}^{13}C/{}^{12}C\right)_{VPDB}} - 1. \quad (1)$$

The $\delta^{13}C$ values were further corrected by a two-point linear correction, based on all measured CAN and CAF values throughout a measurement week. LVal was used as a quality control standard. Repeated measurements of LVal showed good reproducibility (<0.3‰) and accuracy, and $\delta^{13}C$ was found to be nearly independent of the carbon mass.

2.3.2. Radiocarbon

OC, WIOC and EC were converted to CO_2 using our custom-built aerosol combustion system (ACS) following the isolation protocol summarized in Fig. S3. The ACS system and the isolation protocol have been detailed in Dusek et al. (2014) and evaluated in two intercomparison studies (Szidat et al., 2013; Zenker et al., 2017). Interfering gases (e.g., NO_x, halogens and water vapor) were separated from CO_2 in a reduction oven filled with copper grains and silver as well as two water traps (a dry ice-ethanol bath and a flask filled with P_2O_5).

For ^{14}C measurement, the purified CO_2 was subsequently introduced into a gas ion source of the Mini Carbon Dating System (MICADAS) accelerator mass spectrometer by a gas inlet system at CIO (Dee et al., 2019; Aerts-Bijma et al., 2020). ^{14}C data are reported using fraction modern ($F^{14}C$; Reimer et al., 2004):

$$F^{14}C = \frac{\left({}^{14}C/{}^{12}C\right)_{sample,[-25]}}{0.7459 \times \left({}^{14}C/{}^{12}C\right)_{OXII,[-25]}}, \quad (2)$$

where the $^{14}C/^{12}C$ ratio of the oxalic acid standard (OXII) is related to the unperturbed atmosphere in the reference year of 1950 by multiplying it with a factor of 0.7459; the $^{14}C/^{12}C$ ratios of both the sample and OXII are normalized to $\delta^{13}C = -25‰$. The $F^{14}C$ values are corrected for memory effect and for instrument background, which are determined from the measured $F^{14}C$ of standards (OXII with nominal $F^{14}C$ of 1.3407 and Rommenhöller with $F^{14}C$ of 0), followed by normalization to the average value of (memory and background corrected) OXII standards (Wacker et al., 2010). The reliability of the data correction was further verified by measuring a secondary standard (IAEA-C7) in the same measurement series (Aerts-Bijma et al., 2020). The measured values of IAEA-C7 (0.494 ± 0.010) agreed with its consensus value (0.4953 ± 0.0012) within uncertainties.

2.4. ^{14}C-based source apportionment

The $F^{14}C$ of EC, OC and WIOC were directly measured. $F^{14}C$ of WSOC was calculated from mass and $F^{14}C$ of OC and WIOC (Text S2, Table S2). $F^{14}C$ values were converted to the fraction of non-fossil carbon in EC, OC, WIOC and WSOC (f_{bb}(EC), f_{nf}(OC), f_{nf}(WIOC) and f_{nf}(WSOC)) by dividing their corresponding $F^{14}C$ values by $F^{14}C$ of non-fossil sources ($F^{14}C_{nf}$). $F^{14}C_{nf}$ is slightly larger than 1 due to the excess ^{14}C from nuclear bomb tests in the 1960s. $F^{14}C_{nf}$ was estimated as 1.09 ± 0.05 for OC fractions and 1.10 ± 0.05 for EC (see details in Ni et al., 2019b) from a tree growth model and the contemporary atmospheric $^{14}CO_2$ over the past years (Lewis et al., 2004; Mohn et al., 2008; Levin et al., 2010), with the assumption that biomass burning and biogenic emissions contribute to 85% and 15% of total OC, respectively. Knowing the fraction of non-fossil carbon, carbon concentrations were apportioned into carbon from non-fossil sources (EC_{bb}, OC_{nf}, $WIOC_{nf}$, $WSOC_{nf}$) and fossil sources (EC_{fossil}, OC_{fossil}, $WIOC_{fossil}$, $WSOC_{fossil}$) (Eqs. S8–S15 in Table S3). The final uncertainties of the source apportionment results were propagated from uncertainties in mass, $F^{14}C$ and $F^{14}C_{nf}$ of different carbon fractions. The results of the ^{14}C source apportionment are presented in Tables S4 and S5.

3. Results and discussion

3.1. Size-resolved concentrations of carbonaceous aerosol

The size-resolved TC concentrations over the fine particle range (i.e., impactor stages with cut sizes 2.5 μm and below) were investigated with measurements during high, moderate and low $PM_{2.5}$ pollution events. The TC concentrations in $PM_{2.5}$ were low (9 μg m^{-3}) during the low pollution events (LPE), when the air mass originated from the northwest with low RH (35%) and high wind speed (Figs. S1 and S2). Elevated TC concentrations were observed during the moderate pollution event (MPE; 14 μg m^{-3}) and during the high pollution events (HPE; 33 μg m^{-3} for HPE-December and 25 μg m^{-3} for HPE-March). During high and moderate pollution events, air masses were mainly from the west (Fig. S2), transporting relatively clean air to Beijing (An et al., 2019 and references therein). At ambient RH, highest TC concentrations were found in the size range of 0.77–1.4 μm for the two high pollution events, and in the size range of $D_p < 0.25$ μm for moderate and low pollution events (Fig. S1b). The two high pollution events had similar TC size distribution (Fig. 1a), with a geometric mean diameter (GMD) near 0.83 μm and a geometric standard deviation (GSD) of 1.46. TC size distributions for moderate and low pollution events shifted to smaller sizes with GMDs both near 0.70 μm and GSDs of 1.64 and 1.58, respectively, showing broader distribution (i.e., larger GSD) than for high pollution events. The different carbon mass size distributions for different pollution events are related to changes in local and regional sources, atmospheric processes, and meteorological conditions.

Both moderate and low pollution events were characterized by lower RH (~35%) compared to high pollution events (76% for HPE-December and 55% for HPE-March). However, the hygroscopic growth of particles at higher RH cannot fully explain the increased particle size during high pollution events. Converting the GMD at ambient RH to the GMD at dry

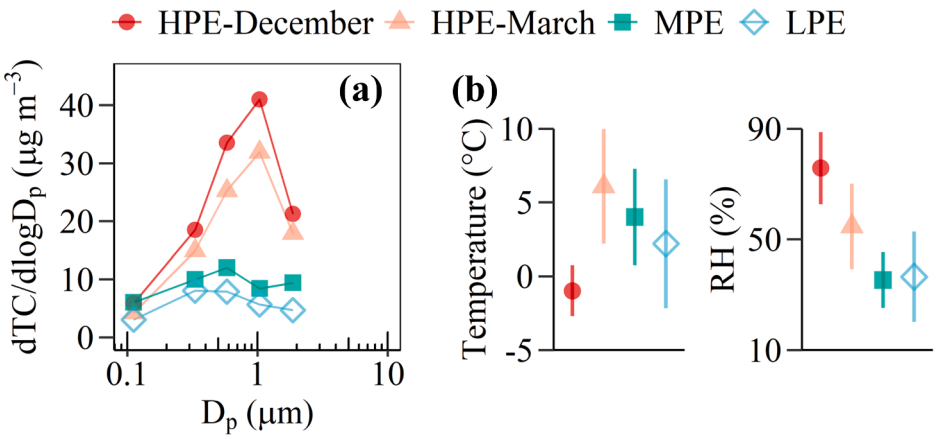

Fig. 1. TC mass size distribution **(a)** and meteorological parameters **(b)** including temperature and relative humidity (RH) during high pollution events (HPE-December and HPE-March), moderate and low pollution events (MPE and LPE, respectively) at an urban site of Beijing. In panel a, the back-up filter is included as a size channel from 0.05 μm to 0.25 μm (Text S3). For details of each sample, also see Section 2.3 and Table S1.

condition using the hygroscopic growth factors reported in previous studies for Beijing (Wang et al., 2018; Ding et al., 2019), the GMD of TC mass at dry condition would be 0.75–0.81 μm for high pollution events, still larger than those for moderate and low pollution events (~0.70 μm). The increased GMD is probably caused by increased SOA formation and condensation on the pre-existing particles and/or aging of carbonaceous aerosols leading to the increase of particle size (Fuzzi et al., 2015; Shrivastava et al., 2017). Size distributions of EC, OC, WIOC and WSOC were very similar to that of TC and high pollution events had a larger GMD and smaller GSD compared to moderate and low pollution events (Fig. S4). At elevated RH during high pollution events, a similar size increase of EC and OC suggests that EC and OC were internally mixed.

3.2. Fossil and non-fossil carbon fractions as a function of particle size

Radiocarbon analysis allows us to unambiguously apportion fossil versus non-fossil source contribution to aerosol carbon, because $F^{14}C$ is not affected by atmospheric processing. Fig. 2 shows the fraction of fossil carbon in EC and OC (f_{fossil}(EC), f_{fossil}(OC)) in Beijing as a function of particle size. The source contributions to EC showed a distinct size dependence, with the highest fossil contribution to particles in the smallest size range (<0.25 μm) and in the largest size range (1.4–2.5 μm) and the highest biomass burning contribution (i.e., lowest f_{fossil}(EC)) in one of the two size ranges of 0.44–0.77 μm and 0.77–1.4 μm. This size dependence was more pronounced during the high pollution events. f_{fossil}(EC) varied from 68% to 84% for HPE-December, and from 62% to

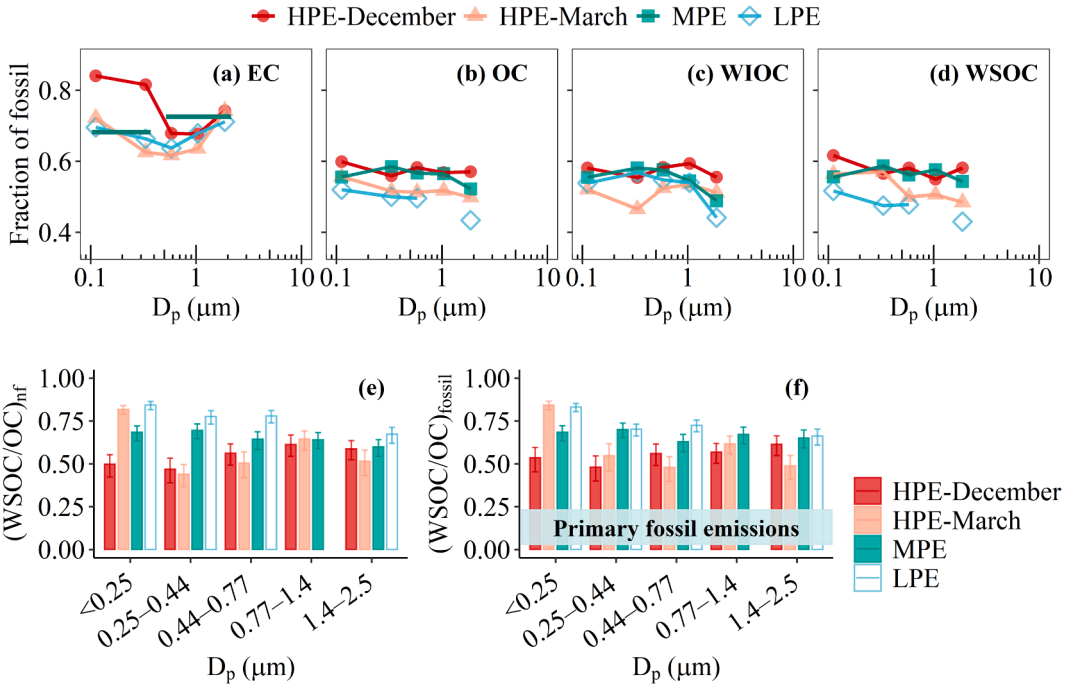

Fig. 2. Fraction of fossil carbon in size-resolved **(a)** EC, **(b)** OC, **(c)** WIOC and **(d)** WSOC as well as size-resolved ratios of **(c)** $(WSOC/OC)_{nf}$ and **(d)** $(WSOC/OC)_{fossil}$ for high, moderate and low pollution events (HPE, MPE and LPE, respectively) during December 2017–March 2018 in urban Beijing. In panel a, some stages of the MPE had to be combined to have enough material for ^{14}C analysis of EC, for these stages, same values are reported and shown as green horizontal bars. In panels e and f, error bars indicate the interquartile range of the median $(WSOC/OC)_{nf}$ and $(WSOC/OC)_{fossil}$. The horizontal dashed area in panel f indicates typical WSOC/OC ratios for primary fossil emissions from vehicular traffic in tunnel studies (Ruellan and Cachier, 2001; Cheung et al., 2009) and residential coal combustion (Yan et al., 2017).

74% for HPE-March. f_{fossil}(EC) values for the low pollution events changed less strongly with particle size, varying from 64% to 71%, a difference of 7%. In contrast to EC, the contribution of fossil sources to OC, WSOC and WIOC did not show a strong size dependence. If OC was dominated by primary sources, f_{fossil}(OC) should show a similar trend as f_{fossil}(EC). This was not the case, indicating that primary sources probably played a minor role and OC was dominated by SOA.

Fossil source contributions to EC were on average 69% (weighted average; range: 62–84%), consistently larger than contributions to OC (55%; 43–60%). Compared with literature ^{14}C data, it is found that our f_{fossil}(EC) values in winter 2018 in urban Beijing were comparable with f_{fossil}(EC) in December 2014 in urban Lhasa (68–76%; Li et al., 2020), and consistently larger than f_{fossil}(EC) in May 2012 in suburb Shanghai (46–58%; Wang et al., 2013) over all particle size ranges. f_{fossil}(OC) values in this study were much larger than those in Lhasa and in Shanghai (28–38%), showing larger fossil contributions to OC in Beijing than in Lhasa and Shanghai. In this study, f_{fossil}(EC) did not differ strongly between high, moderate and low pollution events. However, comparison between the two high pollution events found a moderate difference with higher f_{fossil}(EC) for HPE-December (72%; 68–84%) than for HPE-March (65%; 62–74%), especially in the size ranges of $<$ 0.25 μm and 0.25–0.44 μm. Given that HPE-December had lower average temperatures (−1°C) than HPE-March (6 °C; Fig. 1b), the higher f_{fossil}(EC) for HPE-December could be due to an increased influence of coal combustion for heating in December. Similar to EC, the fossil source contribution to OC was also slightly larger for HPE-December (57%; 56–60%) than for HPE-March (52%; 50–56%). The low pollution events had lower f_{fossil}(OC) (50%; 43–52%) than high and moderate pollution events in all size ranges (Fig. 2b).

The fossil fraction in WSOC during the low pollution events (48%) was slightly lower than that during the other events, which varied between 52% and 57%, averaged over the size ranges. In contrast, f_{fossil}(WIOC) (51% to 58%) was similar for all pollution events. In other words, WSOC (but not WIOC) was more strongly influenced by non-fossil sources during the low pollution events, and this mainly accounted for the lower f_{fossil}(OC) during the low pollution events. During the low pollution events, f_{fossil}(EC) did not decrease, thus the lower f_{fossil}(WSOC) cannot be explained by an increased contribution of primary biomass-burning OC. Cooking OC is mainly water-insoluble (containing e.g., fatty acids and cholesterol; Subramanian et al., 2007), and previous studies showed that in Beijing the biogenic contribution to carbonaceous aerosol is usually low during winter and spring (Zhang et al., 2017). Consequently, lower f_{fossil}(WSOC) during the low pollution events was most likely due to increased contribution of biomass-burning SOA. This conclusion is consistent with the higher $(WSOC/OC)_{nf}$ during the low pollution events compared with the other pollution events in all size ranges (Fig. 2e), associated with the hydrophilic properties of SOA from non-fossil sources (mainly from biomass burning) (Kanakidou et al., 2005; Dusek et al., 2017).

Overall, the fossil source contributions to WIOC (55% with a range of 44–59%) and to WSOC were very similar (54%; 43–62%) (Fig. 2; Table S4). Considering that fossil fuel sources emit only small amounts of primary WSOC (Miyazaki et al., 2006; Weber et al., 2007; Yan et al., 2017), this highlights the importance of secondary aerosol formation from fossil sources in Beijing. This is in line with the consistently larger $(WSOC/OC)_{fossil}$ ratios than WSOC/OC ratios of primary fossil emissions (Fig. 2f), such as emissions from vehicular traffic in tunnel studies (e.g., 0.12 ± 0.05 by Ruellan and Cachier, 2001, 0.06–0.19 by Cheung et al., 2009) and residential coal combustion (0.13 ± 0.10; Yan et al., 2017). The fossil OC was more water-soluble during the low and moderate pollution than during high pollution events, with higher $(WSOC/OC)_{fossil}$ ratios (Fig. 2f). This suggests an enhanced contribution of fossil SOA, likely of regional origin, in addition to the enhanced non-fossil SOA found above. The lower TC concentrations during low and moderate pollution events were likely to contain a larger regional contribution, with enhanced secondary sources (and thus increased WSOC/OC ratios) due to long-range transport. During high pollution events, air masses were mainly from the west (Fig. S2), not from the south where the high polluted regions are (An et al., 2019 and references therein).

The ratios of $(WSOC/OC)_{nf}$ and $(WSOC/OC)_{fossil}$ did not vary strongly with particle size for the low and moderate pollution events, as well as HPE-December. Only HPE-March had a large spread in $(WSOC/OC)_{nf}$ and $(WSOC/OC)_{fossil}$ with highest values in the smallest particle size range (D_p $<$ 0.25 μm). For HPE-March the highest WSOC/OC ratios at D_p $<$ 0.25 μm suggests that the atmospheric conditions (e.g., higher temperature, RH, and solar radiation) during HPE-March may favor the accumulation of organic compounds with higher water-solubility in smaller particle sizes, which might suggest that a predominant aging mechanism is through evaporation, gas-phase oxidation and re-condensation of primary organic compounds.

During high pollution events, fossil and non-fossil OC and EC peaked at the size range of 0.77–1.4 μm, with GMDs of 0.81–0.87 μm (Fig. S5), indicating that OC and EC were internally mixed. Both fossil and non-fossil OC and EC concentrations did not increase in the smallest size range (D_p $<$ 0.25 μm) during high pollution events, but their mass concentrations in the higher size ranges increased strongly (Fig. S5). Since primary sources mainly emit particles in the $<$ 0.25 μm size range, this shows that local primary emissions were not enhanced, but that secondary formation contributed strongly to the particle growth. Both fossil and non-fossil WIOC mass concentrations were enhanced from the second size range (0.25–0.44 μm) compared to the low and moderate pollution events (Fig. 3). However, WSOC concentrations were still comparable in the second size range for all pollution events and enhanced in high pollution events only from the third size range (0.44–0.77 μm) onwards. This clearly shows that production of WSOC was associated with larger particles than WIOC during high pollution events. It has been shown that aqueous-phase chemistry is an important growth mechanism for particles during haze events (Wang et al., 2021). The association of WSOC with larger particle sizes therefore highlights the aqueous-phase chemistry as a possible pathway for production of both fossil and non-fossil OC, especially since photochemical aging would tend to enrich WSOC at smaller particle sizes. During the two high pollution events, non-fossil EC and OC had similar mass size distributions, while mass concentrations of fossil EC and OC during HPE-December were higher

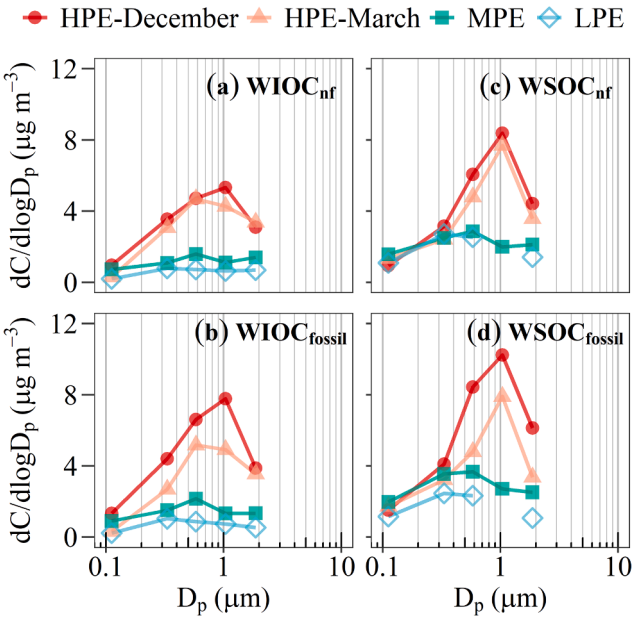

Fig. 3. Size distributions of **(a)** non-fossil WIOC, **(b)** fossil WIOC, **(c)** non-fossil WSOC and **(d)** fossil WSOC during high pollution events (HPE-December and HPE-March), moderate and low pollution events (MPE and LPE, respectively). The back-up filter is included as a size channel from 0.05 μm to 0.25 μm (Text S3). Particle sizes are aerodynamic diameters (D_p).

than those during HPE-March especially in the accumulation mode (Fig. S5). This shows that higher TC concentration during HPE-December (Fig. 1) were mainly caused by increased fossil source contributions. When comparing fossil concentrations in the largest size range (1.4–2.5 μm) for HPE-December and HPE-March, fossil EC was similar. However, significantly higher fossil OC concentrations were observed for HPE-December, mainly caused by enhanced fossil WSOC rather than fossil WIOC. Increased fossil WSOC within this size range was likely a result of enhanced aqueous-phase production of fossil OC that accumulated in the large particle size at higher RH during HPE-December.

In summary, radiocarbon analysis suggests some changes in primary source contributions among different particle sizes and pollution events, as evidenced by differences in f_{fossil}(EC) between particle size ranges and the various pollution events. Secondary sources and chemical processing seemed to dominate OC, resulting in constant f_{fossil}(OC) with particle size and fossil OC that was much more water-soluble than that of primary sources. Both fossil and non-fossil OC and EC concentrations in the smallest size range did not increase during high pollution events, but their mass concentrations in the higher size ranges increased strongly, indicating that OC and EC were internally mixed and that secondary formation / aqueous-phase chemistry processes contributed strongly to the particle growth. Compared with low and moderate pollution events, enhanced WSOC mass during high pollution events was on average associated with larger particles than WIOC, highlighting the aqueous-phase chemistry as an important pathway for production of both fossil and non-fossil OC.

3.3. Stable carbon isotope composition as a function of particle size and thermal refractiveness

In contrast to $F^{14}C$, the $\delta^{13}C$ values are influenced by source signatures as well as by atmospheric processes (i.e., photochemical oxidation and secondary formation) via kinetic isotope effects. As shown in Fig. 4, all the reported $\delta^{13}C_{TC}$ values (−27.0‰ to −23.3‰) fell in the range of aerosol from liquid fossil fuel combustion ($\delta^{13}C_{liq.\ fossil}$ = −25.5‰ ± 1.3‰; mean ± SD), coal combustion ($\delta^{13}C_{coal}$ = −23.4‰ ± 1.3‰) and C3 plant burning ($\delta^{13}C_{C3}$ = −26.7‰ ± 1.8‰; Andersson et al., 2015 and references therein), showing the dominance of anthropogenic sources. Even the most negative $\delta^{13}C_{TC}$ values were more enriched in ^{13}C than $\delta^{13}C$ of biogenic aerosols like α-pinene (−28.4‰ to −29.5‰), monoterpenes (−27.6‰ to − 32.9‰; Haberstroh et al., 2019) and β-pinene (−29.6‰ ± 0.2‰; Fisseha et al., 2009), reflecting a minor contribution from biogenic sources to carbonaceous aerosols. This is in line with our expectations (see Section 3.2) and earlier findings in winter and spring in Beijing (Zhang et al., 2017). On average, the most depleted $\delta^{13}C_{TC}$ values were observed for HPE-December (−25.8‰, weighted average), followed by MPE (−25.4‰), with the more enriched $\delta^{13}C_{TC}$ being observed for

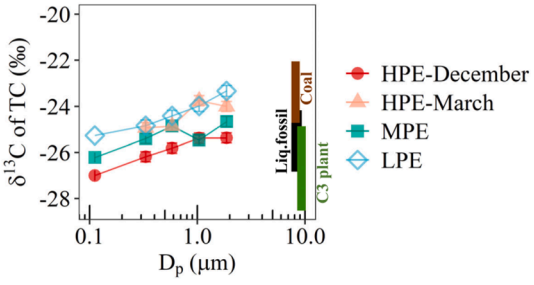

Fig. 4. $\delta^{13}C$ of size-resolved TC during high, moderate and low pollution events (HPE, MPE and LPE, respectively). The error bars indicate the measurement uncertainties of $\delta^{13}C$. The endmember ranges (mean ± SD; see Section 3.3 for details) for coal combustion (brown), liquid fossil fuel combustion (black) and C3 plant burning (green) are indicated as shaded rectangular bars on the right y-axis.

HPE-March (−24.3‰) and LPE (−24.6‰). $\delta^{13}C_{TC}$ increased with increasing particle size. Particles in the smallest size range have short life-times and are therefore mainly locally produced, whereas particles in the larger size range have life-times of days and are of more regional character. The increase in $\delta^{13}C_{TC}$ with particle size can most likely be attributed to sources and atmospheric processing of OC as explained below.

The $\delta^{13}C$ and mass of OC that desorbed at different temperature steps (200 °C, 350 °C and 650 °C) in helium are presented in Fig. 5. The different desorption temperatures roughly correspond to OC with different thermal stabilities, where more volatile OC tends to desorb at lower temperatures and less volatile OC at higher temperatures. It is usually recognized that photochemical or aqueous-phase processing (aging) results in more oxidized, less volatile OC. For example, Masalaite et al. (2020) showed that the mass fraction of less volatile OC was higher in summer than in winter due to active photochemical processing. Overall, OC desorbed at 650 °C ($OC_{650°C}$) accounted for the highest fraction of OC mass for all pollution events, and OC desorbed at 200 °C ($OC_{200°C}$) was the smallest fraction. OC desorbed at 350 °C ($OC_{350°C}$) constituted ~ 30% of total OC at all particle sizes for all pollution events. On the other hand, the mass fraction of $OC_{650°C}$ increased with increasing particle size, indicating that larger particles are more aged.

In terms of isotopic composition, recently formed SOA is considered to be depleted in ^{13}C, whereas photochemical or aqueous-phase aging leads to OC enriched in ^{13}C (Kirillova et al., 2013; Pavuluri and Kawamura, 2016; Dasari et al., 2019). In our samples, $OC_{650°C}$ had the most enriched $\delta^{13}C$ values ($\delta^{13}C_{OC,650}$) of −23.9‰ (weighted average; range: −26.9‰ to −20.3‰), compared to $OC_{350°C}$ ($\delta^{13}C_{OC,350}$ = −25.2‰; −26.6‰ to −23.1‰) and $OC_{200°C}$ ($\delta^{13}C_{OC,200}$ = −26.5‰; −27.2‰ to −25.7‰). In contrast, $\delta^{13}C$ of OC for primary emissions does not change very strongly with increasing desorption temperature (i.e., varying within at most 2‰; Zenker et al., 2020). The most strongly enriched $\delta^{13}C_{OC,650}$ values cannot be explained by primary emissions, because even $\delta^{13}C$ of coal combustion, the most enriched primary source (−21‰ to −25‰; Widory, 2006), is more depleted than the measured $\delta^{13}C_{OC,650}$ (up to −20.3‰). Furthermore, the presence of carbonates ($\delta^{13}C$–0‰) in $OC_{650°C}$ was excluded. Carbonates desorb only at temperature > 550 °C (Huang et al., 2006; Masalaite et al., 2020) and lowering the desorption temperature from 650 °C to 550 °C did not change the $\delta^{13}C$ values within the measurement uncertainties (Fig. S6). The most likely explanation of the strongly enriched $\delta^{13}C_{OC,650}$ is therefore atmospheric aging processes.

$\delta^{13}C_{OC,650}$ values were strongly size-dependent during all pollution events (Fig. 5a), with the most enriched values in the larger size ranges (0.77–2.5 μm), where particles are more regional in origin and, based on the higher mass fraction of $OC_{650°C}$, more aged. The smaller, more local particles contained less $OC_{650°C}$ with lower $\delta^{13}C_{OC,650}$ values. Fig. 6 relates $\delta^{13}C_{OC,650}$ to the mass fraction of $OC_{650°C}$ for different particle sizes during different pollution events. During low and moderate pollution events (LPE and MPE), $\delta^{13}C_{OC,650}$ showed a strong linear correlation with the mass fraction of $OC_{650°C}$, both increasing with the increase of particle size (Fig. 6a). In Section 3.2, we conclude a probable regional influence on LPE and MPE aerosols. The linear relationship strongly supports the hypothesis that atmospheric aging processes are responsible for the enriched $\delta^{13}C$ values of $OC_{650°C}$. In addition, $\delta^{13}C_{OC,650}$ values were most enriched during LPE (range: −24.4‰ to −20.3‰), and most depleted during HPE-December (−26.9‰ to −24.0‰). More enriched $\delta^{13}C_{OC,650}$ values together with higher WSOC/OC ratios during LPE than during other events (Fig. 2) are both consistent with atmospheric aging of OC during long-rang transport (Aggarwal and Kawamura, 2008; Aggarwal et al., 2013; Kirillova et al., 2013; Dasari et al., 2019; Zhang et al., 2019), which further corroborates a larger regional contribution and stronger aging of the LPE aerosol. In contrast, no similar trend was found during high pollution events (Fig. 6b), where regional, aged aerosols probably played a minor role. This is also supported by air mass back trajectories mainly from the west during high pollution events (Fig. S2), not from the south where high polluted regions are (An et al., 2019 and references therein).

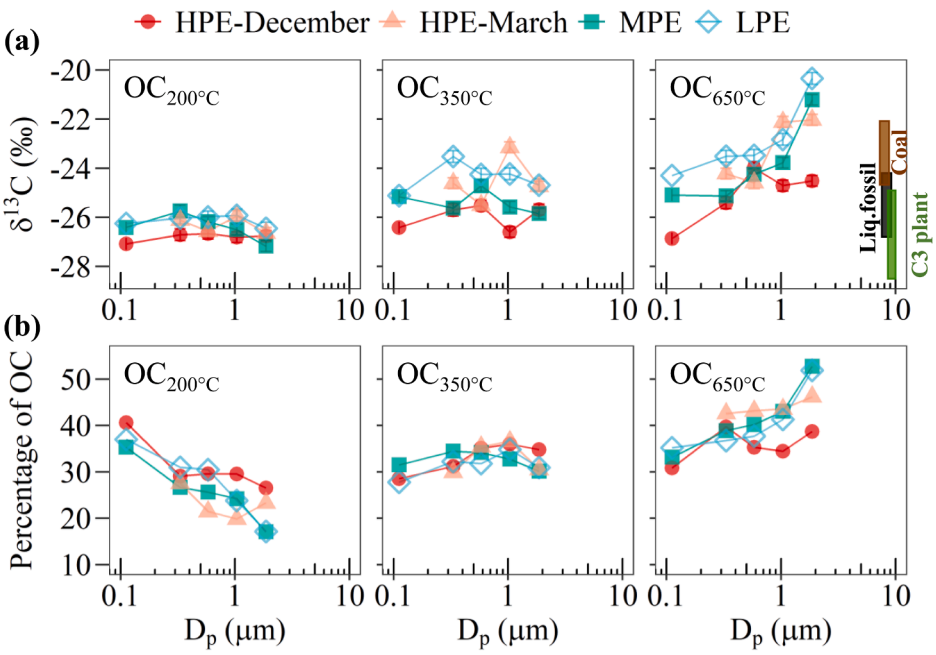

Fig. 5. **(a)** $\delta^{13}C$ of size-resolved OC desorbed at different temperature steps (200 °C, 350 °C and 650 °C) during high, moderate and low pollution events (HPE, MPE and LPE, respectively). The error bars indicate the measurement uncertainties of $\delta^{13}C$. The endmember ranges (mean ± SD; see Section 3.3 for details) for coal combustion (brown), liquid fossil fuel combustion (black) and C3 plant burning (green) are indicated as shaded rectangular bars on the right y-axis. **(b)** Mass percentage of OC desorbed at 200 °C, 350 °C and 650 °C ($OC_{200°C}$, $OC_{350°C}$ and $OC_{650°C}$, respectively) in total desorbed OC for size-resolved aerosols.

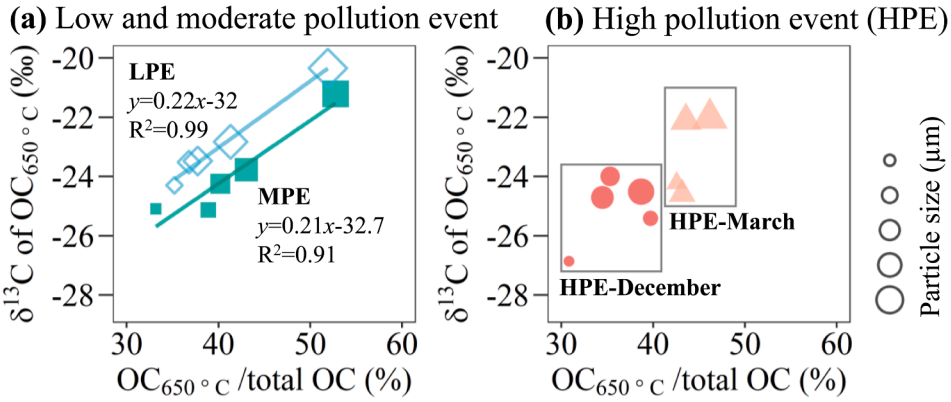

Fig. 6. $\delta^{13}C$ of $OC_{650°C}$ (‰) vs. mass percentage of $OC_{650°C}$ in total desorbed OC (%) during **(a)** low and moderate pollution events (LPE and MPE, respectively) and **(b)** high pollution events (HPE; HPE-December and HPE-March). The symbol size is proportional to the particle size range (<0.25 μm, 0.25–0.44 μm, 0.44–0.77 μm, 0.77–1.4 μm and 1.4–2.5 μm, respectively).

$OC_{200°C}$ has a relatively high mass fraction in primary OA and recently formed SOA and a low mass fraction in aged OA (Vodička et al., 2015; Keller and Burtscher, 2017; Meusinger et al., 2017; Ni et al., 2019a), and is therefore representative of local emission and formation. In contrast to $\delta^{13}C_{OC,650}$, $\delta^{13}C_{OC,200}$ values were more depleted and were similar for all particle size ranges and for different pollution events (all $\delta^{13}C_{OC,200}$ values were within a range of 1.5‰, see Fig. 5a). Depleted $\delta^{13}C_{OC,200}$ values were also found for aerosols at urban, coastal and forest sites in Eastern Europe, and were explained by newly formed SOA (Masalaite et al., 2020) that is depleted with respect to the partially oxidized precursor gases (Irei et al., 2006). The constant $\delta^{13}C_{OC,200}$ values for different pollution events point to local sources of $OC_{200°C}$ and an internal mixture of this local OC and aged regional particles. Previous studies found that primary OA is more volatile than aged OA (Keller and Burtscher, 2017; Vodička et al., 2015). $OC_{200°C}$ could therefore probably arise from small primary particles and end up in larger particles by coagulation. On the other hand, condensation of locally produced SOA on pre-existing particles could also lead to internally mixed $OC_{200°C}$. The decreasing mass fraction of $OC_{200°C}$ with larger sizes (Fig. 5b) is consistent with both hypotheses, but the relatively ^{13}C-depleted $OC_{200°C}$ points to a larger role of SOA. Comparison between the two high pollution events, OC for HPE-December was more volatile (i.e., larger fraction of $OC_{200°C}$ in total desorbed OC) than OC for HPE-March. This could be caused by partitioning of semi-volatile OC to the particle phase due to the lower ambient temperature during HPE-December. In addition, photochemical processing led to less volatile OC and was further enhanced for HPE-March when the ambient temperature was high.

In summary, $\delta^{13}C$ of OC increased with desorption temperature steps (200 °C, 350 °C and 650 °C). The less volatile OC that desorbed at 650 °C ($OC_{650°C}$) was the largest mass fraction in total desorbed OC. Both $\delta^{13}C$ of $OC_{650°C}$ (range: −26.9‰ to −20.3‰) and the large mass fraction of $OC_{650°C}$ increased with the increase of particle size, due to photochemical aging. This is especially evident during low and moderate $PM_{2.5}$ pollution events, when regional, aged aerosol played an important role. In contrast, the relatively low $\delta^{13}C_{OC,200}$ (−27.2‰ to −25.7‰) suggests major contribution of SOA to the more volatile OC desorbed at 200 °C ($OC_{200°C}$). $OC_{200°C}$ showed similar depleted ^{13}C signatures for all particle sizes and for all different pollution events, pointing to an internal mixture of local and aged regional OC.

4. Conclusions

This study presents the first detailed dual-carbon isotopic characterization (i.e., radiocarbon ^{14}C and the stable carbon isotope ^{13}C) of size-resolved OC and EC during high, moderate and low $PM_{2.5}$ pollution events in wintertime Beijing, to elucidate the sources and atmospheric processes of carbonaceous aerosol and therefore one of the important factors driving $PM_{2.5}$ pollution in urban environment. Compared to low and moderate pollution events, fossil and non-fossil OC and EC concentrations during high pollution events did not increase in the smallest size range ($D_p < 0.25$ μm), but increased strongly in the higher size ranges. This shows that local primary emissions were not enhanced, but that secondary formation contributed strongly to the particle growth. The enhanced OC concentrations at higher relative humidity during high pollution events were attributed to both increased fossil and non-fossil WIOC and WSOC, with WSOC concentrating at larger particle sizes than WIOC, highlighting the aqueous-phase chemistry as an important pathway for production of both fossil and non-fossil OC.

Fossil source contributions to EC (weighted average: 69%; range: 62–84%) were consistently larger than contributions to OC (55%; 43–60%), WIOC (55%; 44–59%) and WSOC (54%; 43–62%). The source contribution to EC showed strong size dependence, with the highest fossil contribution to EC in the smallest (<0.25 μm) and largest size range (1.4–2.5 μm), especially during the high pollution events, reflecting changes in primary source contributions among different particle sizes and pollution events. Unlike EC, fossil source contributions to OC, WIOC and WSOC did not show a strong size dependence, indicating that primary sources probably played a minor role and OC was dominated by secondary formation. Secondary OC was largely from fossil sources, evidenced by comparable fossil source contributions to WIOC and to WSOC as well as larger fossil WSOC/OC ratios than WSOC/OC ratios of primary fossil emissions. Larger non-fossil source contributions to OC and WSOC (but not WIOC) was observed during low pollution events, mainly associated with the hydrophilic properties of non-fossil secondary OC from biomass burning.

$\delta^{13}C$ of OC increased strongly with increased desorption temperature steps (200 °C, 350 °C and 650 °C), varying from −26.5‰ to −25.2‰ to –23.9‰ (weighted average). This is in contrast to primary emission for which $\delta^{13}C$ of OC does not change very strongly with increasing desorption temperature. $\delta^{13}C_{OC,650}$ values (range: −26.9‰ to −20.3‰) were more enriched in larger particle size ranges, due to photochemical aging. $\delta^{13}C_{OC,650}$ changed with different pollution events. During low and moderate pollution events, $\delta^{13}C_{OC,650}$ was strongly correlated with the mass fraction of $OC_{650°C}$ in total OC, both increasing with the increase of particle size, reflecting the important role of regional, aged aerosol. Especially for low pollution events, the more enriched $\delta^{13}C_{OC,650}$ and higher WSOC/OC ratios than for other events points to a larger regional contribution and more extensive processing of aged aerosol. In contrast to $\delta^{13}C_{OC,650}$, the relatively low $\delta^{13}C_{OC,200}$ values (−27.2‰ to −25.7‰) were similar for all particle size ranges and for different pollution events, pointing to internal mixture of local and aged regional $OC_{200°C}$. With decreased mass fraction of $OC_{200°C}$ at larger particle sizes, the low $\delta^{13}C_{OC,200}$ values were probably due to the influence of secondary OC formation on the more volatile OC that desorbed at 200 °C. $\delta^{13}C_{TC}$ (−27.0‰ to –23.3‰) fell in the range of anthropogenic aerosols, reflecting minor biogenic contribution to carbonaceous aerosols. Increasing with the increasing particle size, $\delta^{13}C_{TC}$ can most likely be attributed to sources and atmospheric processing of OC.

CRediT authorship contribution statement

Haiyan Ni: Methodology, Validation, Formal analysis, Visualization, Writing – original draft, Writing – review & editing. **Ru-Jin Huang:** Conceptualization, Methodology, Resources, Writing – review & editing, Funding acquisition, Project administration. **Peng Yao:** Methodology, Investigation. **Max M. Cosijn:** Investigation, Validation. **Norbertas Kairys:** Investigation, Validation. **Haobin Zhong:** Investigation, Validation. **Ulrike Dusek:** Conceptualization, Methodology, Resources, Writing – review & editing, Funding acquisition, Project administration.

Declaration of Competing Interest

The authors declare that they have no known competing financial interests or personal relationships that could have appeared to influence the work reported in this paper.

Acknowledgments

This work was supported by the National Key Research and Development Program of China (no. 2017YFC0212701), the National Natural Science Foundation of China (no. 41925015), the Chinese Academy of Sciences (no. ZDBS-LY-DQC001), the Strategic Priority Research Program of Chinese Academy of Sciences (no. XDB40000000), the KNAW (no. 530-5CDP30), and the Cross Innovative Team fund from the State Key Laboratory of Loess and Quaternary Geology (no. SKLLQGTD1801). We thank Dipayan Paul and Marc Bleeker for their help with the ^{14}C measurements. Special thanks are also given to Henk Jansen for his help with the IRMS maintenance at CIO.

Appendix A. Supplementary material

Supplementary data to this article can be found online at https://doi.org/10.1016/j.envint.2021.106890.

References

Aerts-Bijma, A.T., Paul, D., Dee, M.W., Palstra, S.W.L., Meijer, H.A.J., 2021. An independent assessment of uncertainty for radiocarbon analysis with the new generation high-yield accelerator mass spectrometers. Radiocarbon 63 (1), 1–22. https://doi.org/10.1017/RDC.2020.101.

Aggarwal, S.G., Kawamura, K., 2008. Molecular distributions and stable carbon isotopic compositions of dicarboxylic acids and related compounds in aerosols from Sapporo, Japan: implications for photochemical aging during long-range atmospheric transport. J. Geophys. Res. 113, D14301. https://doi.org/10.1029/2007JD009365.

Aggarwal, S.G., Kawamura, K., Umarji, G.S., Tachibana, E., Patil, R.S., Gupta, P.K., 2013. Organic and inorganic markers and stable C-, N-isotopic compositions of tropical coastal aerosols from megacity Mumbai: sources of organic aerosols and atmospheric processing. Atmos. Chem. Phys. 13, 4667–4680. https://doi.org/10.5194/acp-13-4667-2013.

An, Z., Huang, R.-J., Zhang, R., Tie, X., Li, G., Cao, J., Zhou, W., Shi, Z., Han, Y., Gu, Z., Ji, Y., 2019. Severe haze in northern China: a synergy of anthropogenic emissions and atmospheric processes. Proc. Natl. Acad. Sci. U.S.A. 116 (18), 8657–8666. https://doi.org/10.1073/pnas.1900125116.

Andersson, A., Deng, J., Du, K.e., Zheng, M., Yan, C., Sköld, M., Gustafsson, Ö., 2015. Regionally-varying combustion sources of the January 2013 severe haze events over eastern China. Environ. Sci. Technol. 49 (4), 2038–2043. https://doi.org/10.1021/es503855e.

Andersson, A., Kirillova, E.N., Decesari, S., DeWitt, L., Gasore, J., Potter, K.E., Prinn, R. G., Rupakheti, M., de Dieu Ndikubwimana, J., Nkusi, J., Safari, B., 2020. Seasonal source variability of carbonaceous aerosols at the Rwanda Climate Observatory. Atmos. Chem. Phys. 20 (8), 4561–4573. https://doi.org/10.5194/acp-20-4561-2020.

Cavalli, F., Viana, M., Yttri, K.E., Genberg, J., Putaud, J.-P., 2010. Toward a standardised thermal-optical protocol for measuring atmospheric organic and elemental carbon: the EUSAAR protocol. Atmos. Meas. Tech. 3 (1), 79–89. https://doi.org/10.5194/amt-3-79-2010.

Ceburnis, D., Garbaras, A., Szidat, S., Rinaldi, M., Fahrni, S., Perron, N., Wacker, L., Leinert, S., Remeikis, V., Facchini, M.C., Prevot, A.S.H., Jennings, S.G., Ramonet, M., O'Dowd, C.D., 2011. Quantification of the carbonaceous matter origin in submicron marine aerosol by ^{13}C and ^{14}C isotope analysis. Atmos. Chem. Phys. 11, 8593–8606. https://doi.org/10.5194/acp-11-8593-2011.

Cheung, K.L., Polidori, A., Ntziachristos, L., Tzamkiozis, T., Samaras, Z., Cassee, F.R., Gerlofs, M., Sioutas, C., 2009. Chemical characteristics and oxidative potential of particulate matter emissions from gasoline, diesel, and biodiesel cars. Environ. Sci. Technol. 43 (16), 6334–6340. https://doi.org/10.1021/es900819t.

Dasari, S., Andersson, A., Bikkina, S., Holmstrand, H., Budhavant, K., Satheesh, S., Asmi, E., Kesti, J., Backman, J., Salam, A., Bisht, D.S., Tiwari, S., Hameed, Z., Gustafsson, Ö., 2019. Photochemical degradation affects the light absorption of water-soluble brown carbon in the South Asian outflow. Sci. Adv. 5 (1), eaau8066. https://doi.org/10.1126/sciadv.aau8066.

Dee, M.W., Palstra, S.W.L., Aerts-Bijma, A.T., Bleeker, M.O., de Bruijn, S., Ghebru, F., Jansen, H.G., Kuitems, M., Paul, D., Richie, R.R., Spriensma, J.J., Scifo, A., van Zonneveld, D., Verstappen-Dumoulin, B.M.A.A., Wietzes-Land, P., Meijer, H.A.J., 2020. Radiocarbon dating at Groningen: new and updated chemical pretreatment procedures. Radiocarbon 62 (1), 63–74. https://doi.org/10.1017/RDC.2019.101.

Ding, J., Zhang, Y.F., Zhao, P.S., Tang, M., Xiao, Z.M., Zhang, W.H., Zhang, H.T., Yu, Z.J., Du, X., Li, L.W., Yuan, J., Feng, Y.C., 2019. Comparison of size-resolved hygroscopic growth factors of urban aerosol by different methods in Tianjin during a haze episode. Sci. Total Environ. 678, 618–626. https://doi.org/10.1016/j.scitotenv.2019.05.005.

Dusek, U., Meusinger, C., Oyama, B., Ramon, W., de Wilde, P., Holzinger, R., Röckmann, T., 2013. A thermal desorption system for measuring $\delta^{13}C$ ratios on organic aerosol. J. Aerosol Sci. 66, 72–82. https://doi.org/10.1016/j.jaerosci.2013.08.005.

Dusek, U., Monaco, M., Prokopiou, M., Gongriep, F., Hitzenberger, R., Meijer, H.A.J., Röckmann, T., 2014. Evaluation of a two-step thermal method for separating organic and elemental carbon for radiocarbon analysis. Atmos. Meas. Tech. 7, 1943–1955. https://doi.org/10.5194/amt-7-1943-2014.

Dusek, U., Hitzenberger, R., Kasper-Giebl, A., Kistler, M., Meijer, H.A.J., Szidat, S., Wacker, L., Holzinger, R., Röckmann, T., 2017. Sources and formation mechanisms of carbonaceous aerosol at a regional background site in the Netherlands: insights from a year-long radiocarbon study. Atmos. Chem. Phys. 17, 3233–3251. https://doi.org/10.5194/acp-17-3233-2017.

Fisseha, R., Spahn, H., Wegener, R., Hohaus, T., Brasse, G., Wissel, H., Tillmann, R., Wahner, A., Koppmann, R., Kiendler-Scharr, A., 2009. Stable carbon isotope composition of secondary organic aerosol from β-pinene oxidation. J. Geophys. Res. 114, D02304. https://doi.org/10.1029/2008JD011326.

Fuzzi, S., Baltensperger, U., Carslaw, K., Decesari, S., Denier van der Gon, H., Facchini, M.C., Fowler, D., Koren, I., Langford, B., Lohmann, U., Nemitz, E., Pandis, S., Riipinen, I., Rudich, Y., Schaap, M., Slowik, J.G., Spracklen, D.V., Vignati, E., Wild, M., Williams, M., Gilardoni, S., 2015. Particulate matter, air quality and climate: lessons learned and future needs. Atmos. Chem. Phys. 15, 8217–8299. https://doi.org/10.5194/acp-15-8217-2015.

Haberstroh, S., Kreuzwieser, J., Boeddeker, H., Eiblmeier, M., Gutte, H., Lobo-do-Vale, R., Caldeira, M.C., Werner, C., 2019. Natural carbon isotope composition distinguishes compound groups of biogenic volatile organic compounds (BVOC) in two Mediterranean woody species. Front. For. Glob. Change 2, 55. https://doi.org/10.3389/ffgc.2019.00055.

Hallquist, M., Wenger, J.C., Baltensperger, U., Rudich, Y., Simpson, D., Claeys, M., Dommen, J., Donahue, N.M., George, C., Goldstein, A.H., Hamilton, J.F., Herrmann, H., Hoffmann, T., Iinuma, Y., Jang, M., Jenkin, M.E., Jimenez, J.L., Kiendler-Scharr, A., Maenhaut, W., McFiggans, G., Mentel, T.F., Monod, A., Prévôt, A.S.H., Seinfeld, J.H., Surratt, J.D., Szmigielski, R., Wildt, J., 2009. The formation, properties and impact of secondary organic aerosol: current and emerging issues. Atmos. Chem. Phys. 9, 5155–5236. https://doi.org/10.5194/acp-9-5155-2009.

Huang, L., Brook, J.R., Zhang, W., Li, S.M., Graham, L., Ernst, D., Chivulescu, A., Lu, G., 2006. Stable isotope measurements of carbon fractions (OC/EC) in airborne particulate: a new dimension for source characterization and apportionment. Atmos. Environ. 40 (15), 2690–2705. https://doi.org/10.1016/j.atmosenv.2005.11.062.

Huang, R.-J., Zhang, Y., Bozzetti, C., Ho, K.-F., Cao, J.-J., Han, Y., Daellenbach, K.R., Slowik, J.G., Platt, S.M., Canonaco, F., Zotter, P., Wolf, R., Pieber, S.M., Bruns, E.A., Crippa, M., Ciarelli, G., Piazzalunga, A., Schwikowski, M., Abbaszade, G., Schnelle-Kreis, J., Zimmermann, R., An, Z., Szidat, S., Baltensperger, U., Haddad, I.E., Prévôt, A.S.H., 2014. High secondary aerosol contribution to particulate pollution during haze events in China. Nature 514 (7521), 218–222. https://doi.org/10.1038/nature13774.

Iannone, R., Koppmann, R., Rudolph, J., 2010. Stable carbon kinetic isotope effects for the production of methacrolein and methyl vinyl ketone from the gas-phase reactions of isoprene with ozone and hydroxyl radicals. Atmos. Environ. 44 (34), 4135–4141. https://doi.org/10.1016/j.atmosenv.2010.07.046.

Irei, S., Huang, L., Collin, F., Zhang, W., Hastie, D., Rudolph, J., 2006. Flow reactor studies of the stable carbon isotope composition of secondary particulate organic matter generated by OH-radical-induced reactions of toluene. Atmos. Environ. 40 (30), 5858–5867. https://doi.org/10.1016/j.atmosenv.2006.05.001.

Kanakidou, M., Seinfeld, J.H., Pandis, S.N., Barnes, I., Dentener, F.J., Facchini, M.C., Van Dingenen, R., Ervens, B., Nenes, A., Nielsen, C.J., Swietlicki, E., Putaud, J.P., Balkanski, Y., Fuzzi, S., Horth, J., Moortgat, G.K., Winterhalter, R., Myhre, C.E.L., Tsigaridis, K., Vignati, E., Stephanou, E.G., Wilson, J., 2005. Organic aerosol and global climate modelling: a review. Atmos. Chem. Phys. 5 (4), 1053–1123. https://doi.org/10.5194/acp-5-1053-2005.

Keller, A., Burtscher, H., 2017. Characterizing particulate emissions from wood burning appliances including secondary organic aerosol formation potential. J. Aerosol Sci. 114, 21–30. https://doi.org/10.1016/j.jaerosci.2017.08.014.

Kirillova, E.N., Andersson, A., Sheesley, R.J., Kruså, M., Praveen, P.S., Budhavant, K., Safai, P.D., Rao, P.S.P., Gustafsson, Ö., 2013. ^{13}C-and ^{14}C-based study of sources and atmospheric processing of water-soluble organic carbon (WSOC) in South Asian aerosols. J. Geophys. Res. -Atmos. 118 (2), 614–626. https://doi.org/10.1002/jgrd.50130.

Levin, I., Naegler, T., Kromer, B., Diehl, M., Francey, R., Gomez-Pelaez, A., Steele, P., Wagenbach, D., Weller, R., Worthy, D., 2010. Observations and modelling of the global distribution and long-term trend of atmospheric $^{14}CO_2$. Tellus B 62 (1), 26–46. https://doi.org/10.1111/j.1600-0889.2009.00446.x.

Lewis, C.W., Klouda, G.A., Ellenson, W.D., 2004. Radiocarbon measurement of the biogenic contribution to summertime PM-2.5 ambient aerosol in Nashville. TN. Atmos. Environ. 38 (35), 6053–6061. https://doi.org/10.1016/j.atmosenv.2004.06.011.

Li, J., Zeng, Y., Liu, W., Yao, J., Wei, N., Shan, J., 2020. Concentration changes and characteristics of atmospheric carbon particulates in Lhasa. Environ. Chem. 39, 911–919. https://doi.org/10.7524/j.issn.0254-6108.2019092205 (in Chinese).

Masalaite, A., Holzinger, R., Ceburnis, D., Remeikis, V., Ulevičius, V., Röckmann, T., Dusek, U., 2018. Sources and atmospheric processing of size segregated aerosol particles revealed by stable carbon isotope ratios and chemical speciation. Environ. Pollut. 240, 286–296. https://doi.org/10.1016/j.envpol.2018.04.073.

Masalaite, A., Remeikis, V., Zenker, K., Westra, I., Meijer, H.A.J., Dusek, U., 2020. Seasonal changes of sources and volatility of carbonaceous aerosol at urban, coastal and forest sites in Eastern Europe (Lithuania). Atmos. Environ. 225, 117374. https://doi.org/10.1016/j.atmosenv.2020.117374.

Meusinger, C., Dusek, U., King, S.M., Holzinger, R., Rosenørn, T., Sperlich, P., Julien, M., Remaud, G.S., Bilde, M., Röckmann, T., Johnson, M.S., 2017. Chemical and isotopic composition of secondary organic aerosol generated by α-pinene ozonolysis. Atmos. Chem. Phys. 17, 6373–6391. https://doi.org/10.5194/acp-17-6373-2017.

Miyazaki, Y., Kondo, Y., Takegawa, N., Komazaki, Y., Fukuda, M., Kawamura, K., Mochida, M., Okuzawa, K., Weber, R.J., 2006. Time-resolved measurements of water-soluble organic carbon in Tokyo. J. Geophys. Res. 111, D23206. https://doi.org/10.1029/2006JD007125.

Mkoma, S.L., Kawamura, K., Tachibana, E., Fu, P., 2014. Stable carbon and nitrogen isotopic compositions of tropical atmospheric aerosols: sources and contribution from burning of C_3 and C_4 plants to organic aerosols. Tellus B 66 (1), 20176. https://doi.org/10.3402/tellusb.v66.20176.

Mohn, J., Szidat, S., Fellner, J., Rechberger, H., Quartier, R., Buchmann, B., Emmenegger, L., 2008. Determination of biogenic and fossil CO_2 emitted by waste incineration based on $^{14}CO_2$ and mass balances. Bioresour. Technol. 99 (14), 6471–6479. https://doi.org/10.1016/j.biortech.2007.11.042.

Ni, H., Huang, R.-J., Cao, J., Dai, W., Zhou, J., Deng, H., Aerts-Bijma, A., Meijer, H.A.J., Dusek, U., 2019a. High contributions of fossil sources to more volatile organic aerosol. Atmos. Chem. Phys. 19 (15), 10405–10422. https://doi.org/10.5194/acp-19-10405-2019.

Ni, H., Huang, R.-J., Cao, J., Guo, J., Deng, H., Dusek, U., 2019b. Sources and formation of carbonaceous aerosols in Xi'an, China: primary emissions and secondary formation constrained by radiocarbon. Atmos. Chem. Phys. 19 (24), 15609–15628. https://doi.org/10.5194/acp-19-15609-2019.

Ni, H., Huang, R.-J., Cosijn, M.M., Yang, L.u., Guo, J., Cao, J., Dusek, U., 2020. Measurement report: dual-carbon isotopic characterization of carbonaceous aerosol reveals different primary and secondary sources in Beijing and Xi'an during severe haze events. Atmos. Chem. Phys. 20 (24), 16041–16053. https://doi.org/10.5194/acp-20-16041-2020.

Pavuluri, C.M., Kawamura, K., 2016. Enrichment of ^{13}C in diacids and related compounds during photochemical processing of aqueous aerosols: new proxy for organic aerosols aging. Sci. Rep. 6, 36467. https://doi.org/10.1038/srep36467.

Pöschl, U., 2005. Atmospheric aerosols: composition, transformation, climate and health effects. Angew. Chem. Int. Ed. 44 (46), 7520–7540. https://doi.org/10.1002/anie.200501122.

Reimer, P.J., Brown, T.A., Reimer, R.W., 2004. Discussion: reporting and calibration of post-bomb ^{14}C data. Radiocarbon 46, 1299–1304. https://doi.org/10.1017/S0033822200033154.

Ruellan, S., Cachier, H., 2001. Characterisation of fresh particulate vehicular exhausts near a Paris high flow road. Atmos. Environ. 35 (2), 453–468. https://doi.org/10.1016/S1352-2310(00)00110-2.

Schimmelmann, A., Qi, H., Coplen, T.B., Brand, W.A., Fong, J., Meier-Augenstein, W., Kemp, H.F., Toman, B., Ackermann, A., Assonov, S., Aerts-Bijma, A.T., Brejcha, R., Chikaraishi, Y., Darwish, T., Elsner, M., Gehre, M., Geilmann, H., Gröning, M., Hélie, J.-F., Herrero-Martín, S., Meijer, H.A.J., Sauer, P.E., Sessions, A.L., Werner, R. A., 2016. Organic reference materials for hydrogen, carbon, and nitrogen stable isotope-ratio measurements: caffeines, n-alkanes, fatty acid methyl esters, glycines, L-valines, polyethylenes, and oils. Anal. Chem. 88, 4294–4302. https://doi.org/10.1021/acs.analchem.5b04392.

Shrivastava, M., Cappa, C.D., Fan, J., Goldstein, A.H., Guenther, A.B., Jimenez, J.L., Kuang, C., Laskin, A., Martin, S.T., Ng, N.L., Petaja, T., Pierce, J.R., Rasch, P.J., Roldin, P., Seinfeld, J.H., Shilling, J., Smith, J.N., Thornton, J.A., Volkamer, R., Wang, J., Worsnop, D.R., Zaveri, R.A., Zelenyuk, A., Zhang, Q.i., 2017. Recent advances in understanding secondary organic aerosol: implications for global climate forcing. Rev. Geophys. 55 (2), 509–559. https://doi.org/10.1002/2016RG000540.

Song, C., He, J., Wu, L., Jin, T., Chen, X., Li, R., Ren, P., Zhang, L., Mao, H., 2017. Health burden attributable to ambient $PM_{2.5}$ in China. Environ. Pollut. 223, 575–586. https://doi.org/10.1016/j.envpol.2017.01.060.

Subramanian, R., Donahue, N.M., Bernardo-Bricker, A., Rogge, W.F., Robinson, A.L., 2007. Insights into the primary–secondary and regional–local contributions to organic aerosol and $PM_{2.5}$ mass in Pittsburgh. Pennsylvania. Atmos. Environ. 41 (35), 7414–7433. https://doi.org/10.1016/j.atmosenv.2007.05.058.

Szidat, S., Bench, G., Bernardoni, V., Calzolai, G., Czimczik, C.I., Derendorp, L., Dusek, U., Elder, K., Fedi, M.E., Genberg, J., Gustafsson, Ö., Kirillova, E., Kondo, M., McNichol, A.P., Perron, N., Santos, G.M., Stenström, K., Swietlicki, E., Uchida, M., Vecchi, R., Wacker, L., Zhang, Y.L., Prévôt, A.S.H., 2013. Intercomparison of ^{14}C analysis of carbonaceous aerosols: exercise 2009. Radiocarbon 55 (3), 1496–1509. https://doi.org/10.1017/S0033822200048426.

Tao, J., Zhang, L., Cao, J., Zhang, R., 2017. A review of current knowledge concerning $PM_{2.5}$ chemical composition, aerosol optical properties and their relationships across China. Atmos. Chem. Phys. 17, 9485–9518. https://doi.org/10.5194/acp-17-9485-2017.

Vodička, P., Schwarz, J., Cusack, M., Ždímal, V., 2015. Detailed comparison of OC/EC aerosol at an urban and a rural Czech background site during summer and winter. Sci. Total Environ. 518–519, 424–433. https://doi.org/10.1016/j.scitotenv.2015.03.029.

Vodička, P., Kawamura, K., Schwarz, J., Kunwar, B., Ždímal, V., 2019. Seasonal study of stable carbon and nitrogen isotopic composition in fine aerosols at a Central European rural background station. Atmos. Chem. Phys. 19 (6), 3463–3479. https://doi.org/10.5194/acp-19-3463-2019.

Wacker, L., Christl, M., Synal, H.-A., 2010. Bats: a new tool for AMS data reduction. Nucl. Instrum. Methods Phys. Res. B 268 (7-8), 976–979. https://doi.org/10.1016/j.nimb.2009.10.078.

Wang, G., Yao, J., Zeng, Y., Huang, Y.u., Qian, Y., Liu, W., Li, Y., Yuan, N., Liu, S., Shan, J., 2013. Source apportionment of carbonaceous particulate matter in a Shanghai suburb based on carbon isotope composition. Aerosol Sci. Tech. 47 (3), 239–248. https://doi.org/10.1080/02786826.2012.743959.

Wang, J., Ye, J., Zhang, Q., Zhao, J., Wu, Y., Li, J., Liu, D., Li, W., Zhang, Y., Wu, C., Xie, C., Qin, Y., Lei, Y., Huang, X., Guo, J., Liu, P., Fu, P., Li, Y., Lee, H.C., Choi, H., Zhang, J., Liao, H., Chen, M., Sun, Y., Ge, X., Martin, S.T., Jacob, D.J., 2021. Aqueous production of secondary organic aerosol from fossil-fuel emissions in winter Beijing haze. Proc. Natl. Acad. Sci. U.S.A. 118, e2022179118. https://doi.org/10.1073/pnas.2022179118.

Wang, X., Shen, X.J., Sun, J.Y., Zhang, X.Y., Wang, Y.Q., Zhang, Y.M., Wang, P., Xia, C., Qi, X.F., Zhong, J.T., 2018. Size-resolved hygroscopic behavior of atmospheric aerosols during heavy aerosol pollution episodes in Beijing in December 2016. Atmos. Environ. 194, 188–197. https://doi.org/10.1016/j.atmosenv.2018.09.041.

Wang, Y., Zhang, R., Saravanan, R., 2014. Asian pollution climatically modulates mid-latitude cyclones following hierarchical modelling and observational analysis. Nat. Commun. 5, 3098. https://doi.org/10.1038/ncomms4098.

Weber, R.J., Sullivan, A.P., Peltier, R.E., Russell, A., Yan, B., Zheng, M., de Gouw, J., Warneke, C., Brock, C., Holloway, J.S., Atlas, E.L., Edgerton, E., 2007. A study of secondary organic aerosol formation in the anthropogenic-influenced southeastern United States. J. Geophys. Res. 112, D13302. https://doi.org/10.1029/2007JD008408.

Widory, D., 2006. Combustibles, fuels and their combustion products: a view through carbon isotopes. Combust. Theory Model. 10 (5), 831–841. https://doi.org/10.1080/13647830600720264.

Wu, X., Vu, T.V., Shi, Z., Harrison, R.M., Liu, D., Cen, K., 2018. Characterization and source apportionment of carbonaceous $PM_{2.5}$ particles in China - A review. Atmos. Environ. 189, 187–212. https://doi.org/10.1016/j.atmosenv.2018.06.025.

Yan, C., Zheng, M., Bosch, C., Andersson, A., Desyaterik, Y., Sullivan, A.P., Collett, J.L., Zhao, B., Wang, S., He, K., Gustafsson, Ö., 2017. Important fossil source contribution to brown carbon in Beijing during winter. Sci. Rep. 7 (1), 43182. https://doi.org/10.1038/srep43182.

Zenker, K., Vonwiller, M., Szidat, S., Calzolai, G., Giannoni, M., Bernardoni, V., Jedynska, A.D., Henzing, B., Meijer, H.A.J., Dusek, U., 2017. Evaluation and inter-comparison of oxygen-based OC-EC separation methods for radiocarbon analysis of ambient aerosol particle samples. Atmosphere 8, 226. https://doi.org/10.3390/atmos8110226.

Zenker, K., Sirignano, C., Riccio, A., Chianese, E., Calfapietra, C., Prati, M.V., Masalaite, A., Remeikis, V., Mook, E., Meijer, H.A.J., Dusek, U., 2020. $\delta^{13}C$ signatures of organic aerosols: Measurement method evaluation and application in a source study. J. Aerosol Sci. 145, 105534. https://doi.org/10.1016/j.jaerosci.2020.105534.

Zhang, R., Wang, G., Guo, S., Zamora, M.L., Ying, Q.i., Lin, Y., Wang, W., Hu, M., Wang, Y., 2015a. Formation of urban fine particulate matter. Chem. Rev. 115 (10), 3803–3855. https://doi.org/10.1021/acs.chemrev.5b00067.

Zhang, Y., Ren, H., Sun, Y., Cao, F., Chang, Y., Liu, S., Lee, X., Agrios, K., Kawamura, K., Liu, D., Ren, L., Du, W., Wang, Z., Prevot, A.S.H., Szidat, S., Fu, P., 2017. High contribution of non-fossil sources to sub-micron organic aerosols in Beijing. China. Environ. Sci. Technol. 51, 7842–7852. https://doi.org/10.1021/acs.est.7b01517.

Zhang, Y.-L., Huang, R.-J., El Haddad, I., Ho, K.-F., Cao, J.-J., Han, Y., Zotter, P., Bozzetti, C., Daellenbach, K.R., Canonaco, F., Slowik, J.G., Salazar, G., Schwikowski, M., Schnelle-Kreis, J., Abbaszade, G., Zimmermann, R., Baltensperger, U., Prévôt, A.S.H., Szidat, S., 2015b. Fossil vs. non-fossil sources of fine carbonaceous aerosols in four Chinese cities during the extreme winter haze episode of 2013. Atmos. Chem. Phys. 15 (3), 1299–1312. https://doi.org/10.5194/acp-15-1299-2015.

Zhang, W., Zhang, Y.-L., Cao, F., Xiang, Y., Zhang, Y., Bao, M., Liu, X., Lin, Y.-C., 2019. High time-resolved measurement of stable carbon isotope composition in water-soluble organic aerosols: method optimization and a case study during winter haze in eastern China. Atmos. Chem. Phys. 19 (17), 11071–11087. https://doi.org/10.5194/acp-19-11071-2019.

Zimnoch, M., Morawski, F., Kuc, T., Samek, L., Bartyzel, J., Gorczyca, Z., Skiba, A., Rozanski, K., 2020. Summer–winter contrast in carbon isotope and elemental composition of total suspended particulate matter in the urban atmosphere of Krakow, Southern Poland. Nukleonika 65, 181–191. https://doi.org/10.2478/nuka-2020-0029.